

# Large Pockels effect in micro- and nanostructured barium titanate integrated on silicon

Stefan Abel <sup>ID 1,7\*</sup>, Felix Eltes <sup>ID 1,7</sup>, J. Elliott Ortmann <sup>2</sup>, Andreas Messner <sup>ID 3</sup>, Pau Castera <sup>4</sup>, Tino Wagner <sup>ID 5</sup>, Darius Urbonas <sup>1</sup>, Alvaro Rosa <sup>4</sup>, Ana M. Gutierrez <sup>4</sup>, Domenico Tulli <sup>ID 6</sup>, Ping Ma <sup>ID 3\*</sup>, Benedikt Baeuerle <sup>ID 3</sup>, Arne Josten <sup>ID 3</sup>, Wolfgang Heni <sup>ID 3</sup>, Daniele Caimi <sup>1</sup>, Lukas Czornomaz <sup>1</sup>, Alexander A. Demkov <sup>2</sup>, Juerg Leuthold <sup>ID 3</sup>, Pablo Sanchis <sup>ID 4\*</sup> and Jean Fompeyrine <sup>ID 1</sup>

**The electro-optical Pockels effect is an essential nonlinear effect used in many applications. The ultrafast modulation of the refractive index is, for example, crucial to optical modulators in photonic circuits. Silicon has emerged as a platform for integrating such compact circuits, but a strong Pockels effect is not available on silicon platforms. Here, we demonstrate a large electro-optical response in silicon photonic devices using barium titanate. We verify the Pockels effect to be the physical origin of the response, with  $r_{42} = 923 \text{ pm V}^{-1}$ , by confirming key signatures of the Pockels effect in ferroelectrics: the electro-optic response exhibits a crystalline anisotropy, remains strong at high frequencies, and shows hysteresis on changing the electric field. We prove that the Pockels effect remains strong even in nanoscale devices, and show as a practical example data modulation up to  $50 \text{ Gbit s}^{-1}$ . We foresee that our work will enable novel device concepts with an application area largely extending beyond communication technologies.**

Silicon photonics has become a platform for dense and low-cost integrated photonic circuits for a wide range of applications<sup>1–5</sup>, all of which require fast, energy-efficient electro-optical (EO) switches. State-of-the-art modulators based on silicon<sup>6</sup> rely on the plasma dispersion effect<sup>7</sup> and have two major constraints. First, the change in the real and imaginary parts of the refractive index is linked. Modulation of only the optical phase is therefore not possible, which renders the use of advanced modulation formats difficult<sup>8,9</sup>. Second, the operating speed is limited by the charge-carrier lifetimes in forward-biased devices or by the *RC* characteristics in reversed-biased devices<sup>10</sup>, leading to a maximal bandwidth of a few tens of gigahertz. These constraints are not present in discrete modulators that exploit the Pockels effect in lithium niobate ( $\text{LiNbO}_3$ , LNO) single crystals, which have been used for decades in long-haul telecommunication<sup>11</sup>. Because no Pockels effect exists in a centrosymmetric crystal such as silicon, materials with sizeable Pockels coefficients must be integrated onto silicon photonic structures to combine the benefits of bulk Pockels modulators with the low fabrication costs of integrated silicon photonics. Unfortunately, so far, no satisfactory solution exists. The integration of LNO on silicon can only be performed locally<sup>12</sup> or on small wafer scales<sup>13</sup>, because no epitaxial deposition process is available. Organic materials with large Pockels coefficients have been integrated on silicon and show high-speed performance<sup>14,15</sup>. Unfortunately, their limited range of operating temperatures hinders their use in real applications. Lead zirconate titanate (PZT) thin films, a more stable material, have also been used to fabricate active switches on a SiN waveguide platform<sup>16</sup>, but no direct integration on compact silicon photonics has been achieved.

Barium titanate ( $\text{BaTiO}_3$ , BTO), for several reasons, has emerged as an excellent candidate to enable Pockels-effect-based devices on

silicon. First, BTO has one of the largest Pockels coefficients of all materials<sup>17</sup>. Second, it has previously been used in thin-film EO modulators on exotic oxide substrates<sup>18,19</sup>. Third, BTO can be grown on silicon substrates<sup>20,21</sup> with large wafer sizes, and with excellent crystal quality<sup>22</sup>. Indeed, previous work has reported values of the Pockels coefficients lower than BTO bulk values, but five times larger than bulk LNO<sup>20</sup>. Fourth, BTO is a chemically and thermally stable material. Finally, functional passive photonic structures, such as low-loss hybrid BTO–Si waveguides, have already been realized<sup>23</sup>. Results have been presented on EO switching in BTO–Si waveguides<sup>22,24,25</sup> or in BTO plasmonic devices operated at high speed<sup>26</sup>, but the influence of undesired effects, such as charge migration or plasma dispersion, could not be excluded as the source of the EO response. No proof exists that BTO maintains its superior EO properties when embedded into micro- and nanoscale silicon photonics structures.

In this Article, we unambiguously prove the presence of the Pockels effect in BTO integrated into silicon photonic devices by verifying three independent criteria. We show (1) high-speed modulation up to frequencies of 65 GHz, (2) the dependence of the EO response on the orientation of the optical and externally applied electrical fields relative to the crystalline orientation of BTO and (3) optical evidence of ferroelectric domain switching. These features are unique signatures of the Pockels effect and exclude other physical switching mechanisms. We extract a Pockels coefficient of  $r_{42} \sim 923 \text{ pm V}^{-1}$ , which is 30 times larger than in LNO, and the highest value reported in silicon photonic structures.

In the following sections, we first disclose the fabrication of the layer stack containing ferroelectric BTO, in which the Pockels effect is present. Next, we describe the layout and design of both microscale photonic and nanoscale plasmonic devices to verify

<sup>1</sup>IBM Research—Zurich, Rüschlikon, Switzerland. <sup>2</sup>Department of Physics, The University of Texas, Austin, TX, USA. <sup>3</sup>ETH Zurich, Institute of Electromagnetic Fields (IEF), Zürich, Switzerland. <sup>4</sup>Nanophotonics Technology Center, Universitat Politècnica València, Valencia, Spain. <sup>5</sup>ETH Zurich, Nanotechnology Group, Rüschlikon, Switzerland. <sup>6</sup>DAS Photonics, Universitat Politècnica València, Valencia, Spain. <sup>7</sup>These authors contributed equally: Stefan Abel, Felix Eltes \*e-mail: [sab@zurich.ibm.com](mailto:sab@zurich.ibm.com); [ping.ma@ief.ee.ethz.ch](mailto:ping.ma@ief.ee.ethz.ch); [pabsanki@ntc.upv.es](mailto:pabsanki@ntc.upv.es)

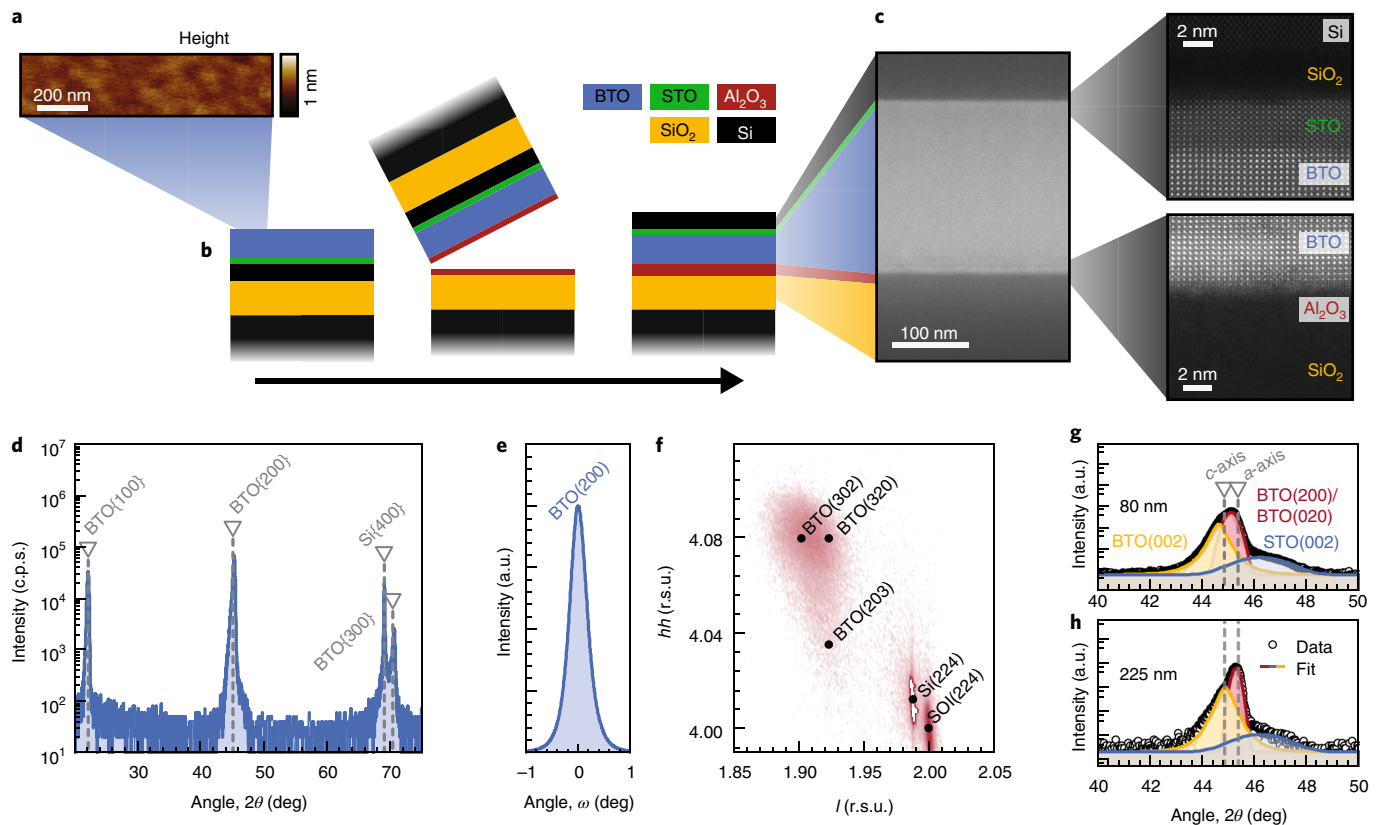


**Fig. 1 | Fabrication process and structural characterization for a hybrid crystalline-amorphous BTO-SiO<sub>2</sub> heterostructure.** **a**, Atomic force microscopy image showing the low roughness of BTO before the bonding process. **b**, Schematic of the process (from left to right) to obtain the hybrid stack using direct wafer bonding of an MBE-grown BTO film onto a thermally oxidized acceptor wafer with Al<sub>2</sub>O<sub>3</sub> as a bonding interface. **c**, Low-resolution cross-sectional image (left), showing a uniform and smooth layer stack, and higher-resolution HRSTEM images (right), revealing the high quality of the crystalline structure of BTO and of the BTO-STO interface formed during the deposition process (right, top) as well as the sharpness of the bonding interface (right, bottom). **d**, HRXRD diffractogram, confirming the absence of any polycrystalline domains in the final hybrid stack, with only BTO (*h*00) peaks visible (pseudo-cubic notation), and the epitaxial relationship between silicon and BTO. **e**, The high quality of the BTO layer is evidenced by the low mosaicity ( $\Delta\omega \approx 0.3^\circ$ ) extracted from the rocking curve measured on the BTO (200) Bragg peak. **f**, Reciprocal space map plotted in reciprocal space units (r.s.u.) around the {224} silicon and {203} BTO Bragg peaks acquired on the hybrid stack. Three possible orientations are revealed, with the long *c* axis being parallel to either the [001] (*c*-axis domains) or [110] or [-110] silicon directions (*a*-axis domains). **g,h**, Higher-resolution diffraction around the pseudo-cubic (200) BTO peak, highlighting the relative contributions of the *a*- and *c*-axis domains in the BTO layer. The comparison of an 80-nm-thick (**g**) and a 225-nm-thick (**h**) BTO layer shows the higher relative fraction of the *c*-axis domain in thinner films.

the presence of the Pockels effect. We then discuss the need to use two complementary device geometries to fully characterize the EO properties of BTO. Finally, we demonstrate the generic applicability of BTO-enhanced photonic structures by performing data modulation at high rates of up to 50 Gbit s<sup>-1</sup>.

### Fabrication of BTO layers

In this section, we show that high-quality, single-crystalline BTO on SiO<sub>2</sub> can be obtained using a combination of epitaxy and direct wafer bonding. With our concept, two prerequisites to enable EO switching in BTO-Si structures are fulfilled: (1) the approach yields dense, crystalline and tetragonal BTO films, which are needed to preserve the Pockels effect<sup>27</sup>; (2) it enables a thick lower cladding below the BTO films, which is required to avoid optical leakage into the substrate. Previous EO BTO-Si devices were based on BTO on silicon-on-insulator (SOI) substrates<sup>24,25</sup>. However, in such layer stacks, mobile charges in the semiconducting device silicon layer may screen the applied electric field and result in an EO response due to plasma dispersion<sup>17</sup>. To prevent this effect, we fabricated a hybrid amorphous-epitaxial heterostructure without any silicon below the BTO layer using a two-step process.

In the first step, 80- to 225-nm-thick BTO layers were grown by molecular beam epitaxy (MBE) on SOI substrates. To ensure epitaxial growth, the SOI was covered with a 4-nm-thin MBE-grown strontium titanate (SrTiO<sub>3</sub>, STO) buffer layer<sup>20</sup> (see Methods). In the second step, we transferred the BTO layer onto another silicon wafer covered with SiO<sub>2</sub> via direct wafer bonding and substrate back-etching, using Al<sub>2</sub>O<sub>3</sub> as the bonding interface<sup>28</sup>. The 5- to 10-nm-thick Al<sub>2</sub>O<sub>3</sub> layer deposited on both the host and the donor wafer via atomic layer deposition guarantees a high bonding strength<sup>29</sup>. The low surface roughness below 0.4 nm for both wafers (Fig. 1a) results in a high bonding yield. After thermal treatment, the donor wafer was removed via grinding and multiple etching steps (see Methods), resulting in the desired wafer stack of Si/STO/BTO/Al<sub>2</sub>O<sub>3</sub>/SiO<sub>2</sub>/Si (Fig. 1b). Most of these steps are commonly available in a back-end-of-the-line integration process and enable the addition of functional oxide layers with planarized, oxide-covered wafers fabricated in a standard CMOS process<sup>22</sup>.

The layers show a well-defined crystalline orientation with respect to the wafer, as is necessary for obtaining high-performance photonic devices<sup>30</sup>. The crystallinity and interfaces remain of high quality after completion of the process, as is visible at a microscopic

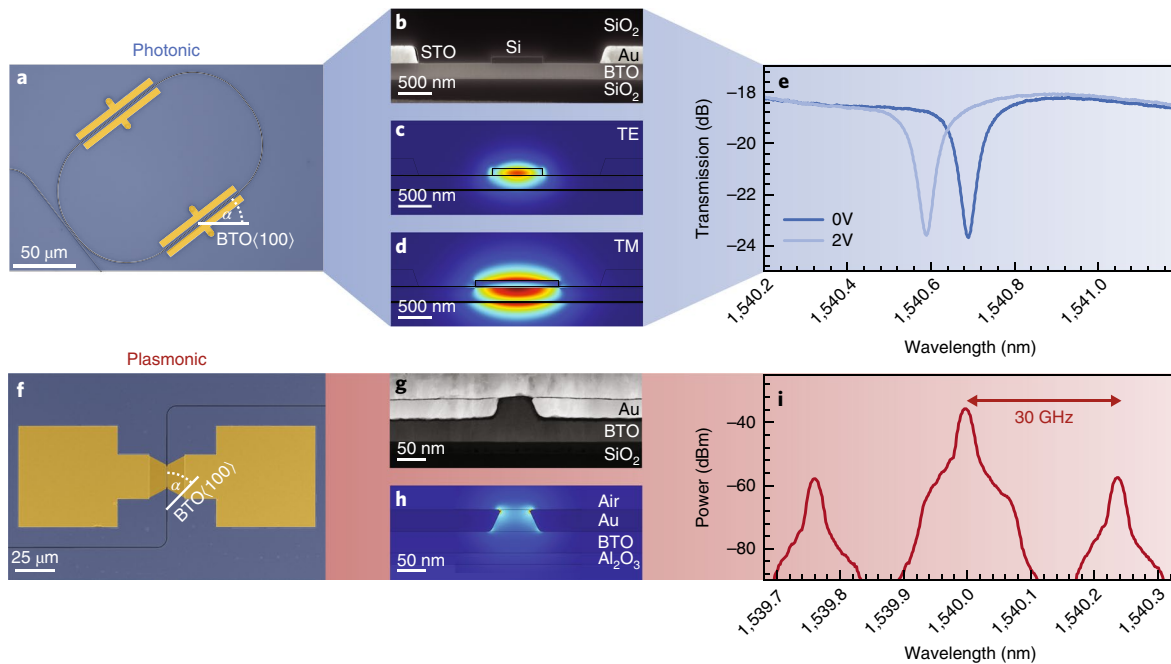


**Fig. 2 | Layout of the photonic and plasmonic devices.** **a**, False-colour optical microscopy image of a photonic ring resonator before fabrication of contact pads. Angle  $\alpha$  indicates the orientation of the straight section relative to the BTO  $<100>$  axis (pseudo-cubic notation). Waveguides are shown in black, the BTO surface in blue, and the electrodes in yellow. **b**, Scanning electron microscopy (SEM) cross-sectional image of the photonic devices between the electrodes. **c,d**, Simulated mode profiles of the photonic TE (**c**) and TM (**d**) modes, respectively (see Methods). The colours indicate the electric field strength, ranging from blue (low) to red (high). **e**, Exemplary transmission spectra of a photonic racetrack resonator for two different bias voltages. The EO response is calculated based on the shift of the resonance wavelength. **f–h**, Similar figures to **a–d** for the plasmonic device, showing the false-coloured top view recorded via SEM (**f**), the cross-section (**g**) and the simulated mode profile (**h**, same colour code as in **c** and **d**). **i**, Example of a transmission spectrum of a plasmonic phase modulator operated at a wavelength of  $\lambda=1,540\text{ nm}$  with a radiofrequency signal at 30 GHz. The intensity ratio of the peak ( $\lambda=1,540.00\text{ nm}$ ) to the first sidebands ( $\lambda=1,539.75\text{ nm}$  and  $1,540.24\text{ nm}$ ) is used to determine the change of the effective index  $\Delta n_{\text{eff}}$  of the plasmonic mode.

level in high-resolution scanning transmission electron microscopy (HRSTEM) images (Fig. 1c). High-resolution X-ray diffraction (HRXRD) analysis confirms the cube-on-cube epitaxial relationship between the BTO layer and the device silicon layer (Fig. 1d). The sharp rocking curve (Fig. 1e) further confirms the high crystal-line quality at a macroscopic level.

A more detailed analysis shows that the BTO film has a tetragonal symmetry, consistent with the bulk unit cell of BTO, with two short  $a$  axes and one longer  $c$  axis (Fig. 1f). The orientation of these axes is critical for device operation because of the strong dependence of the Pockels effect on the relative orientation of the static electric field, the direction and polarization of the light, and the crystalline orientation<sup>20,30</sup>. A reciprocal space map around the BTO(203) film peak (Fig. 1f) shows the presence of two types of  $a$ -axis-oriented domain, rotated by  $90^\circ$  in-plane relative to each other, and a smaller fraction of  $c$ -axis domains (Fig. 1 caption). The  $c$ -axis domains stem from epitaxial strain, and are expected to form at the interface between STO and BTO<sup>20,31</sup>. Consistently, the relative volume fraction of  $c$ -axis domains is larger in the 80 nm thin film (Fig. 1g) than in the 225 nm thick film (Fig. 1h).

### Device integration and characterization

To confirm the Pockels effect in the BTO layer, we tested the anisotropy and frequency behaviour of the EO response of various integrated devices. We used racetrack resonators with differently oriented straight sections relative to the BTO crystalline axes (Fig. 2a). The relatively small footprint of the structures ( $\sim 100\text{ }\mu\text{m} \times 100\text{ }\mu\text{m}$ ) allowed the fabrication of many separate devices of different orientation, which are needed to probe the angular dependence of the EO response. Resonant devices are well studied and allow a quantitative

analysis of the EO response<sup>32</sup>. Due to the finite photon lifetime, the EO bandwidth of resonant photonic devices is typically limited to a few tens of gigahertz<sup>33</sup>, which restricts the usage of such devices for high-speed characterization, as needed to validate the Pockels effect. Mach-Zehnder modulators (MZMs) can be operated at high speed without bandwidth limitations due to the finite photon lifetimes. However, the larger size of MZMs of several millimetres impacts the electrode bandwidth<sup>10</sup>. Advanced radiofrequency engineering of travelling-wave electrodes is required to obtain high-bandwidth BTO-Si-based MZM structures. As an alternative, plasmonic phase modulators offer extremely high bandwidth due to the low capacitance resulting from the small device size<sup>34</sup>. In our work, we used such BTO-based plasmonic structures to extend the frequency range of our EO characterization to 65 GHz. Because an accurate quantitative analysis of plasmonic phase modulators is not possible (Supplementary Note 1), we used both photonic and plasmonic device types for our analysis of the EO response.

We have thus fabricated both photonic and plasmonic devices with embedded BTO (see Methods). For photonic structures, the device silicon layer is used to form strip-loaded waveguides with SiO<sub>2</sub> cladding. The waveguide is single-mode and supports transverse electric (TE) (Fig. 2c) and transverse magnetic (TM) (Fig. 2d) polarizations with 39% (TE) or 55% (TM) of the optical power confined in the BTO layer. Electrodes separated by 2  $\mu\text{m}$  from the waveguide generate an electric field parallel to the 225-nm-thick BTO layer (Fig. 2a,b and Supplementary Note 2). To analyse the tensorial nature of the EO response, racetrack resonators were fabricated with different angles  $\alpha$  relative to the BTO  $<100>$  pseudo-cubic crystalline direction (Fig. 2a). Applying a d.c. or radiofrequency signal to the electrodes (Fig. 2e), the shift in the resonance wavelength of the

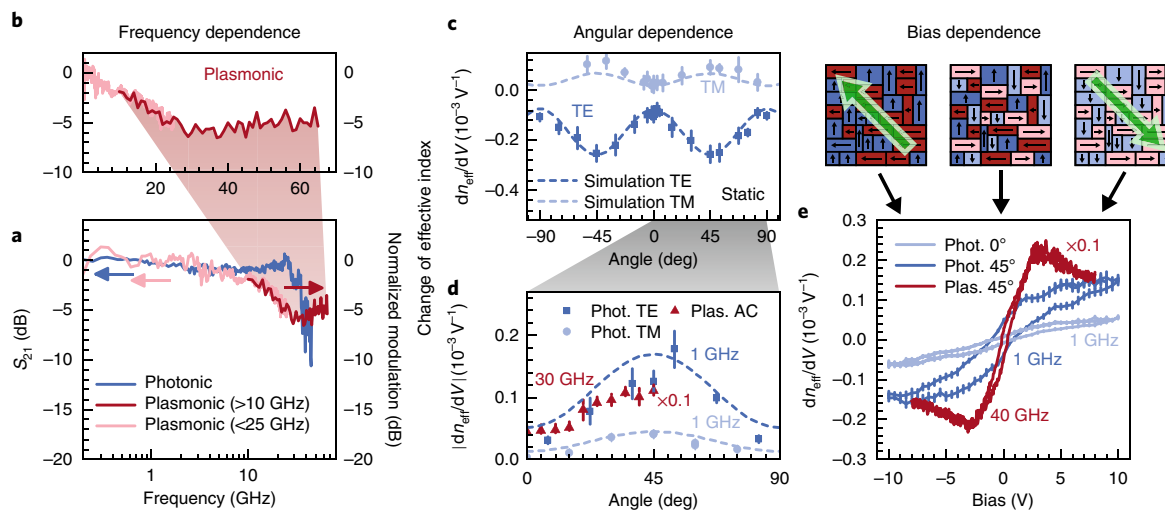


**Fig. 3 | EO response proving the presence of the Pockels effect.** **a**, Frequency dependence of the EO response of a photonic ring modulator (TE polarization) and a plasmonic phase modulator. **b**, Linear magnification of the high-frequency region of the plasmonic modulator up to 65 GHz. **c,d**, Angular dependence of the EO response of photonic devices designed for different optical polarizations for static electric fields (**c**) and for photonic and plasmonic devices under alternating electric (a.c.) fields at 1 GHz and 30 GHz, respectively (**d**). Dashed lines in **c** and **d** correspond to the simulated response of photonic devices using the Pockels tensor extracted from the experiments (Supplementary Note 5). **e**, EO hysteresis curve obtained at 1 GHz (photonic devices, TE polarization) and at 40 GHz (plasmonic devices) when sweeping the applied bias in devices oriented at different angles  $\alpha$  (see labels). The schematics on top indicate the orientation of the ferroelectric domains for the electric field (green arrow) oriented at  $\alpha = \pm 45^\circ$ .

resonators is used to determine the change of the effective mode index  $\Delta n_{\text{eff}}$  in the waveguides (see Methods).

The 10- $\mu\text{m}$ -long plasmonic structures are based on an 80-nm-thick BTO layer, from which a 50-nm-wide fin is etched and contacted (see Methods). The plasmonic waveguide (Fig. 2f,g), confining 50% of the optical power in the BTO layer (Fig. 2h)<sup>35</sup>, is coupled to photonic waveguides via tapered structures (Supplementary Note 3). We derive  $\Delta n_{\text{eff}}$  from the power ratio between spectral bands (Fig. 2i), which are created by two-wave mixing processes on applying a radiofrequency signal to the electrodes (see Methods).

### Confirmation of the Pockels effect

To confirm the presence of the Pockels effect in BTO, it is crucial to analyse the characteristic features of the EO response<sup>36</sup>, primarily its frequency dependence (to exclude slow EO effects) and its anisotropic nature (to rule out isotropic EO effects). In addition, the Pockels effect in a ferroelectric should translate into a hysteretic response of the refractive index versus field, consistent with the poling of ferroelectric domains. Here, we investigate all these characteristics to confirm the presence of the Pockels effect in our devices.

Modulation of the refractive index at radiofrequencies<sup>37</sup> differentiates the Pockels effect from the thermo-optic effect and from ionic diffusion processes, both of which occur at long timescales. We measure a constant EO response up to 30 GHz in photonic devices with Q factors of  $5 \times 10^3$  (Fig. 3a), which coincides with the cutoff frequency of our experimental equipment (see Methods and Supplementary Fig. 22). Due to the finite photon lifetime<sup>33</sup> and peaking effects<sup>38</sup> in resonant structures, the response at higher frequencies cannot be interpreted unambiguously. From the constant EO response up to 30 GHz in photonic devices, we cannot completely exclude a possible contribution of plasma dispersion induced by the strong electric field in the silicon strip above the BTO layer. Non-resonant plasmonic devices, where silicon is absent in the active region, are used to extend the analysis to higher frequencies. Indeed, the EO response in plasmonic devices is constant in the frequency range from 30 to 65 GHz (Fig. 3a), and unambiguously supports the presence of the Pockels effect in BTO-based devices.

In contrast to the flat frequency response of the photonic devices, the plasmonic modulators show a reduction in the EO response in the frequency range from ~2 to 30 GHz by ~5 dB (Fig. 3b). This reduction is attributed to the mechanical boundary conditions in plasmonic devices: at frequencies up to a few gigahertz, horizontal deformation of the BTO fin driven by the piezo-electric effect<sup>39</sup> results in a larger, unclamped EO response<sup>40</sup> compared to the high-frequency region. Such an effect is not visible in photonic devices, where mechanical motion is suppressed due to clamping from the  $\text{SiO}_2$  cladding (Supplementary Note 4).

Because of the tensorial nature of the Pockels effect<sup>40</sup>, the orientation  $\alpha$  of the waveguides (defined in Fig. 2) should influence the EO response. Indeed, photonic racetrack devices show a clear dependence on  $\alpha$  (Fig. 3c). As the electric-field-induced  $\Delta n_{\text{eff}}$  parallel and perpendicular to the BTO layer is anisotropic, the EO response is expected to be sensitive to the polarization of the optical mode. We experimentally confirmed such an anisotropy between the TE and the TM modes in photonic devices (Fig. 3c,d), and compared it with simulations (Supplementary Note 5) of the expected EO response. The experimental angular dependence and polarization dependence of the EO response agree quantitatively with the simulations (Fig. 3c). We determined the two largest non-vanishing coefficients of the Pockels tensor in the BTO layer in the photonic structures to be  $r_{42} = 923 \pm 215 \text{ pm V}^{-1}$  and  $r_{33} = 342 \pm 93 \text{ pm V}^{-1}$ . Owing to the small response of the TM devices at  $\alpha = 0^\circ$ , no reliable extraction of the  $r_{13}$  coefficient is possible (Supplementary Note 6). The similar angular dependences of the EO modulation at static and radiofrequencies indicate a common and constant physical effect as the origin of the EO response at all time and length scales probed in our measurements (Fig. 3d). Here, we limited the analysis to 1 GHz to minimize the influence of finite photon lifetimes on the angular dependence (Supplementary Fig. 21). Our experimental procedure does not allow an accurate quantitative analysis of the Pockels response at radiofrequencies (see Methods). However, the flat frequency response of the  $S_{21}$  parameter in the photonic devices (Fig. 3a) indicates a constant Pockels effect from static (Fig. 3c) to high frequencies (Fig. 3d).

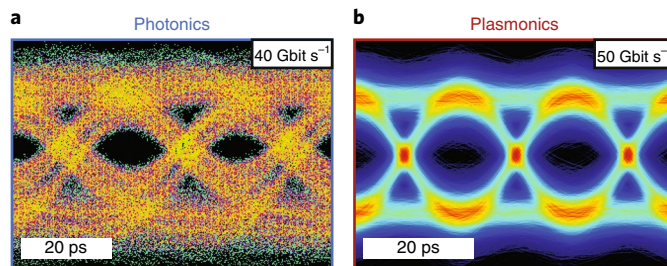


**Fig. 4 | Data transmission in a photonic and plasmonic modulator.** **a,b,** Eye diagrams for data rates of  $40 \text{ Gbit s}^{-1}$  (photonic device) and  $50 \text{ Gbit s}^{-1}$  (plasmonic device) (**b**).

Although we can measure an effective, orientation-dependent materials response in plasmonic devices, which qualitatively agrees well with the tensorial nature of the Pockels effect (Fig. 3d and Supplementary Note 1), it is not possible to deconvolute and quantify the Pockels coefficients as can be done for photonic devices. Nanoscale plasmonic devices are more sensitive to extrinsic effects such as process damages or device geometry, as well as intrinsic effects such as a dead dielectric layer, or the distribution of  $c$ - and  $a$ -axis domains in the plasmonic waveguide. Nevertheless, taking these effects into account, the measured effective response of the plasmonic devices can be reproduced using the Pockels coefficients determined on the photonic devices (Supplementary Note 1).

In addition to the high-frequency response and the angular dependence, the EO response caused by the BTO layer should lead to a hysteretic behaviour when sweeping the bias voltage due to the reorientation of ferroelectric domains. Because the Pockels effect is a linear EO effect, domains with opposing ferroelectric orientations induce an opposite phase shift, resulting in a vanishing EO response for films with equally distributed domains<sup>20</sup>. The EO response will saturate while increasing the bias once all domains are polarized in the same direction. Indeed, the expected hysteresis is clearly visible in both the microscale photonic and nanoscale plasmonic devices (Fig. 3e). The coercive field  $E_c$  extracted for photonic devices ( $E_c = 2 \times 10^5 \text{ V m}^{-1}$ ) is in good agreement with previously reported values for BTO films on silicon of similar thicknesses<sup>20</sup>. In contrast, the coercive field in plasmonic structures is more than one order of magnitude larger ( $E_c = 1 \times 10^7 \text{ V m}^{-1}$ ), but remains consistent with a voltage drop over an interfacial non-ferroelectric layer (Supplementary Note 1) as well as common observations in thin ferroelectrics, where domain pinning and finite depolarizing fields enhance  $E_c$  in devices with reduced dimensions<sup>41</sup>.

In the case of photonic devices, the hysteresis loop is not completely pinched at larger voltages due to slow ionic diffusion processes occurring at timescales similar to the sweeping rate used during the hysteresis measurements (see Methods and Supplementary Note 7). These diffusion effects are related to the surface reactivity of the bonded material stack towards the ambient atmosphere, which take place in the gap between the electrode and the waveguide. As a consequence, the potential distribution within the device is slightly modified without impacting the angular dependence and the frequency response, as discussed above (Supplementary Note 7).

### Application of the Pockels effect

Having demonstrated the existence of a strong Pockels effect in our structures, we now demonstrate its potential use for high-speed data communication (Fig. 4). Recording an eye diagram is an insightful way to evaluate the performance of an EO modulator. A photonic ring modulator with  $Q = 9 \times 10^3$  and a 10-μm-long plasmonic phase modulator with a slot width of 50 nm are used to achieve a high modulation bandwidth (see Methods), with data rates of  $40 \text{ Gbit s}^{-1}$  (photonic device; see Supplementary Fig. 24 for eye diagrams at

lower data rates) and  $50 \text{ Gbit s}^{-1}$  (plasmonic device). These results show the applicability of the BTO-Si technology for high-speed data transmission. They can also be used to estimate the performance of MZMs, which, if well engineered, are commonly preferred over resonant structures or phase modulators for integrated optical links. The EO response measured in our TE photonic waveguides translates to a  $V_\pi L$  product of  $0.45 \text{ V cm}$  (Supplementary Note 8), which is competitive with state-of-the-art integrated Si (ref. <sup>42</sup>) and InP (ref. <sup>43</sup>) EO phase shifters. Additionally, we estimated the switching energy of an optimized MZM (Supplementary Note 8) to be  $96 \text{ fJ}$  per bit, which is in the same range as advanced Si-based MZMs<sup>44,45</sup>. These performance metrics prove the technological relevance of having the Pockels effect available on silicon as an EO switching mechanism.

### Conclusion

We have unambiguously demonstrated the presence of the Pockels effect in a hybrid  $\text{BaTiO}_3\text{-SiO}_2$  stack integrated into photonic and plasmonic structures on silicon. While the photonic resonator devices allow for the quantitative determination of the individual Pockels tensor elements of BTO, the plasmonic devices enable bandwidth measurements at frequencies up to 65 GHz. The results from these two complementary device structures demonstrate that BTO maintains its superior EO properties after fabrication of both microscale photonic and nanoscale plasmonic components. Key characteristics, such as the high-speed response, the angular anisotropy and hysteretic switching rule out other physical effects as the origin of the EO response. The magnitude of the EO response is bulk-like<sup>40</sup> and many times larger than for any Pockels materials previously integrated on silicon<sup>12,16,20</sup>. The chemical and thermal stabilities of oxides also outperform those of organic nonlinear materials<sup>15,46</sup>.

The use of our structures for data communication at rates of  $50 \text{ Gbit s}^{-1}$  reveals the prospects of this technology for a new class of integrated modulators. Our approach can deliver devices with a competitive  $V_\pi L$ , is suited for complex modulation formats, and is compatible with a tight integration within CMOS fabrication lines. Having demonstrated the presence of the Pockels effect in the materials stack, we foresee that superior EO performance can be obtained by further optimization of device parameters such as the thickness of the BTO layer, the gap between the electrodes, and with the electrode layout optimized for radiofrequency operation.

The ability to control the Pockels effect in integrated photonic devices also has profound implications for applications beyond data communication. Sensory<sup>5,47,48</sup>, mid-infrared<sup>49</sup> and neuromorphic computing applications<sup>3,4,50</sup> would also strongly benefit from devices that are operated at reduced operating speeds or exploit non-volatile EO effects. Ultimately, hybrid BTO-Si photonic devices provide an additional degree of freedom for designers to realize not only a new generation of compact, high-speed modulators, but also novel devices such as ultralow-power tuning elements<sup>25</sup>, non-volatile optical memories<sup>51</sup> or microwave-to-optical quantum converters<sup>52</sup>.

### Online content

Any methods, additional references, Nature Research reporting summaries, source data, statements of data availability and associated accession codes are available at <https://doi.org/10.1038/s41563-018-0208-0>.

Received: 15 November 2017; Accepted: 26 September 2018;  
Published online: 12 November 2018

### References

- Hochberg, M. & Baehr-Jones, T. Towards fabless silicon photonics. *Nat. Photon.* **4**, 492–494 (2010).
- Reed, G. T., Mashanovich, G., Gardes, F. Y. & Thomson, D. J. Silicon optical modulators. *Nat. Photon.* **4**, 518–526 (2010).
- Shen, Y. et al. Deep learning with coherent nanophotonic circuits. *Nat. Photon.* **1**, 441–446 (2017).

4. Vandoorne, K. et al. Experimental demonstration of reservoir computing on a silicon photonics chip. *Nat. Commun.* **5**, 3541 (2014).
5. Leinders, S. M. et al. A sensitive optical micro-machined ultrasound sensor (OMUS) based on a silicon photonic ring resonator on an acoustical membrane. *Sci. Rep.* **5**, 14328 (2015).
6. Reed, G. T. et al. Recent breakthroughs in carrier depletion based silicon optical modulators. *Nanophotonics* **3**, 229–245 (2014).
7. Soref, R. A. & Bennett, B. R. Electrooptical effects in silicon. *IEEE J. Quantum Electron.* **23**, 123–129 (1987).
8. Zalehpour, S., Lin, J. & Rusch, L. in *International Photonics Conference of the IEEE TuH2.3* (IEEE, 2017).
9. Xu, K. et al. Compatibility of silicon Mach-Zehnder modulators for advanced modulation formats. *J. Lightwave Technol.* **31**, 2550–2554 (2013).
10. Petousi, D. et al. Analysis of optical and electrical tradeoffs of traveling-wave depletion-type Si Mach-Zehnder modulators for high-speed operation. *IEEE J. Sel. Top. Quantum Electron.* **21**, 3400108 (2015).
11. Janner, D., Tulli, D., García-Granda, M., Belmonte, M. & Pruneri, V. Micro-structured integrated electro-optic LiNbO<sub>3</sub> modulators. *Laser Photon. Rev.* **3**, 301–313 (2009).
12. Chen, L., Xu, Q., Wood, M. G. & Reano, R. M. Hybrid silicon and lithium niobate electro-optical ring modulator. *Optica* **1**, 112–118 (2014).
13. Rabiei, P., Ma, J., Khan, S., Chiles, J. & Fathpour, S. Heterogeneous lithium niobate photonics on silicon substrates. *Opt. Express* **21**, 25573 (2013).
14. Leuthold, J. et al. Silicon-organic hybrid electro-optical devices. *IEEE J. Sel. Top. Quantum Electron.* **19**, 3401413 (2013).
15. Heni, W. et al. Silicon-organic and plasmonic-organic hybrid photonics. *ACS Photonics* **4**, 1576–1590 (2017).
16. Alexander, K. et al. Nanophotonic Pockels modulators on a silicon nitride platform. *Nat. Commun.* **9**, 3444 (2018).
17. Abel, S. & Fompeyrine, J. in *Thin Films on Silicon* Vol. 8 (eds. Narayanan, V., Frank, M. M. & Demkov, A. A.) 455–501 (World Scientific, Singapore, 2016).
18. Petraru, A., Schubert, J., Schmid, M., Trithaveesak, O. & Buchal, C. Integrated optical Mach-Zehnder modulator based on polycrystalline BaTiO<sub>3</sub>. *Opt. Lett.* **28**, 2527–2529 (2003).
19. Girouard, P. et al.  $\chi^{(2)}$  Modulator with 40 GHz modulation utilizing BaTiO<sub>3</sub> photonic crystal waveguides. *IEEE J. Quantum Electron.* **53**, 5200110 (2017).
20. Abel, S. et al. A strong electro-optically active lead-free ferroelectric integrated on silicon. *Nat. Commun.* **4**, 1671 (2013).
21. Meier, A. R., Niu, F. & Wessels, B. W. Integration of BaTiO<sub>3</sub> on Si (001) using MgO/STO buffer layers by molecular beam epitaxy. *J. Cryst. Growth* **294**, 401–406 (2006).
22. Eltes, F. et al. in *Proceedings of IEEE International Electron Devices Meeting (IEDM)* 601–604 (IEEE, 2017).
23. Eltes, F. et al. Low-loss BaTiO<sub>3</sub>-Si waveguides for nonlinear integrated photonics. *ACS Photonics* **3**, 1698 (2016).
24. Xiong, C. et al. Active silicon integrated nanophotonics: ferroelectric BaTiO<sub>3</sub> devices. *Nano Lett.* **14**, 1419–1425 (2014).
25. Abel, S. et al. A hybrid barium titanate-silicon photonics platform for ultraefficient electro-optic tuning. *J. Lightwave Technol.* **34**, 1688–1693 (2016).
26. Messner, A. et al. in *Proceedings of 2017 Optical Fiber Communications Conference and Exhibition, OFC 2017* 7–9 (OSA, 2017).
27. Kormondy, K. J. et al. Microstructure and ferroelectricity of BaTiO<sub>3</sub> thin films on Si for integrated photonics. *Nanotechnology* **28**, 075706 (2017).
28. Czornomaz, L. et al. Scalability of ultra-thin-body and BOX InGaAs MOSFETs on silicon. In *2013 Proceedings of European Solid-State Device Research Conference (ESSDERC)* 143–146 (IEEE, 2013).
29. Czornomaz, L. et al. Wafer bonding: an integration route for hybrid III-V/SiGe CMOS on 300mm. *ECS Trans.* **64**, 199–209 (2014).
30. Castera, P. et al. Electro-optical modulation based on Pockels effect in BaTiO<sub>3</sub> with a multi-domain structure. *IEEE Photon. Technol. Lett.* **28**, 990–993 (2016).
31. Dubourdieu, C. et al. Switching of ferroelectric polarization in epitaxial BaTiO<sub>3</sub> films on silicon without a conducting bottom electrode. *Nat. Nanotech.* **8**, 748–754 (2013).
32. Bogaerts, W. et al. Silicon microring resonators. *Laser Photon. Rev.* **6**, 47–73 (2012).
33. Li, G. et al. 25 Gb/s 1V-driving CMOS ring modulator with integrated thermal tuning. *Opt. Express* **19**, 20435 (2011).
34. Hoessbacher, C. et al. Plasmonic modulator with >170 GHz bandwidth demonstrated at 100 Gb/s NRZ. *Opt. Express* **25**, 1762 (2017).
35. Brosi, J., Koos, C., Andreani, L. C., Leuthold, J. & Freude, W. Modulator with a polymer-infiltrated silicon photonic crystal waveguide. *Opt. Express* **16**, 180–185 (2008).
36. Borghi, M. et al. Homodyne detection of free carrier induced electro-optic modulation in strained silicon resonators. *J. Lightwave Technol.* **34**, 5657–5668 (2016).
37. Marcus, R. B. (ed.) *Measurement of High-Speed Signals in Solid State Devices. Semiconductors and Semimetals* Vol. 28 (Academic Press, New York, 1990).
38. Müller, J. et al. Optical peaking enhancement in high-speed ring modulators. *Sci. Rep.* **4**, 6310 (2014).
39. Zhou, Q., Lau, S., Wu, D. & Kirk Shung, K. Piezoelectric films for high frequency ultrasonic transducers in biomedical applications. *Prog. Mater. Sci.* **56**, 139–174 (2011).
40. Bernasconi, P., Zgonik, M. & Gunter, P. Temperature dependence and dispersion of electro-optic and elasto-optic effect in perovskite crystals. *J. Appl. Phys.* **78**, 2651–2658 (1995).
41. Rabe, K. M., Ahn, C. H. & Triscone, J.-M. (eds) *Physics of Ferroelectrics* Vol. 105 (Springer, Berlin, 2007).
42. Patel, D. et al. Design, analysis, and transmission system performance of a 41 GHz silicon photonic modulator. *Opt. Express* **23**, 14263 (2015).
43. Rouvalis, E. in *Proceedings of 2015 IEEE Compound Semiconductor Integrated Circuit Symposium, CSICS 2015* 1–4 (2015); <https://doi.org/10.1109/CSICS.2015.7314513>
44. Baehr-Jones, T. et al. Ultralow drive voltage silicon traveling-wave modulator. *Opt. Express* **20**, 12014 (2012).
45. Ding, J. et al. *Mach-Zehnder silicon optical modulator*. **20**, 59–63 (2012).
46. Haffner, C. et al. All-plasmonic Mach-Zehnder modulator enabling optical high-speed communication at the microscale. *Nat. Photon.* **9**, 525–528 (2015).
47. Zhang, Y., Han, R. & Xiang, T. Application of non-contact optic voltage sensor based on Pockels effect in  $\pm 800$  kV convertor station. In *2016 IEEE International Conference on High Voltage Engineering and Application (ICHVE)*, 1–4 (IEEE, 2016).
48. Stan, N., Seng, E., Shumway, L., King, R. & Schultz, S. Non-perturbing voltage measurement in a coaxial cable with slab-coupled optical sensors. *Appl. Opt.* **56**, 6814–6821 (2017).
49. Jin, T. et al. Monolithic mid-infrared integrated photonics using silicon-on-epitaxial barium titanate thin films. *ACS Appl. Mater. Interfaces* **9**, 21848–21855 (2017).
50. Abel, S., Stark, D. J., Eltes, F., Caimi, D. & Fompeyrine, J. in *IEEE International Conference of Rebooting Computing 2017* (IEEE, 2017); <https://doi.org/10.1109/ICRC.2017.8123672>
51. Ríos, C. et al. Integrated all-photonic non-volatile multi-level memory. *Nat. Photon.* **9**, 725–732 (2015).
52. Javerzac-Galy, C. et al. On-chip microwave-to-optical quantum coherent converter based on a superconducting resonator coupled to an electro-optic microresonator. *Phys. Rev. A* **94**, 053815 (2016).

## Acknowledgements

This project received funding from the European Commission under grant agreement nos FP7-ICT-2013-11-619456 (SITOGA), H2020-ICT-2015-25-688579 (PHRESCO), 688282 (PETMEM) and H2020-ICT-2017-1-780997 (plaCMOS), from the Swiss State Secretariat for Education, Research and Innovation under contract nos 15.0285 and 16.0001, and from the Swiss National Foundation project no. 200021\_159565 (PADOMO). J.E.O. and A.A.D. acknowledge support from the Air Force Office of Scientific Research under grant FA9550-12-10494 and from the National Science Foundation under grant no. IRES-1358111. J.E.O. is grateful for generous support from the National Science Foundation Graduate Research Fellowship under grant no. DGE-1610403. P.S. acknowledges funding from project TEC2016-76849 (MINECO/FEDER, UE).

## Author contributions

S.A., F.E. and J.F. fabricated and structurally characterized the epitaxial BTO and STO layers. S.A., J.F. and P.S. defined the photonics device concept (photonics), and P.M., J.L. and J.F. the plasmonics concept. The concepts were refined and implemented by S.A. and F.E. (photonics) and by A.M., F.E. and P.M. (plasmonics). S.A., D.C. and F.E. fabricated the photonic devices and F.E. the plasmonic devices. S.A., J.E.O. (as a visiting scientist at IBM) and L.C. characterized the EO performance of the photonic devices. P.C., A.R., A.M.G. and J.E.O. performed the data communication experiments on the photonic structures and analysed the data together (with P.S. and D.T.). A.M., F.E., A.J., B.B. and W.H. characterized the EO performance of plasmonic devices and analysed the data. F.E. performed all TEM investigations. T.W. and S.A. performed and analysed the KFM experiments. D.U., J.E.O. and S.A. performed the simulation of the photonic devices. A.M. performed the simulations of the plasmonic devices. S.A., F.E. and J.F. wrote the manuscript, with the support of all authors. S.A., P.M., P.S. and A.D. bear responsibility for the contributions to the manuscript emanating from their team.

## Competing interests

The authors declare no competing interests.

## Additional information

**Supplementary information** is available for this paper at <https://doi.org/10.1038/s41563-018-0208-0>.

**Reprints and permissions information** is available at [www.nature.com/reprints](http://www.nature.com/reprints).

**Correspondence and requests for materials** should be addressed to S.A. or P.M. or P.S. **Publisher's note:** Springer Nature remains neutral with regard to jurisdictional claims in published maps and institutional affiliations.

© The Author(s), under exclusive licence to Springer Nature Limited 2018

## Methods

**Fabrication of BTO layers.** *MBE deposition.* MBE deposition was performed in a chamber with a base pressure of  $<3 \times 10^{-10}$  torr. Before BTO deposition on 2-inch SOI wafers with 100- or 220-nm-thick device silicon layers, a 4-nm STO seed layer was deposited. After HF-cleaning of the substrate, 0.5 monolayers of Sr were deposited at 600–650 °C. After cooling to 50 °C, the Sr was oxidized in molecular oxygen, followed by deposition of amorphous STO at an O<sub>2</sub> pressure of  $\sim 5 \times 10^{-7}$  torr. The amorphous STO was crystallized by annealing in ultrahigh vacuum (UHV) at 400–500 °C, resulting in epitaxial STO. BTO growth was carried out at 500–600 °C under atomic oxygen. A plasma source was used to generate atomic oxygen at a pressure of  $\sim 5 \times 10^{-6}$  torr.

**Bonding.** Direct wafer bonding was performed using 5- to 10-nm-thick Al<sub>2</sub>O<sub>3</sub> layers deposited by atomic layer deposition on both donor and receiver wafers. After surface preparation and bonding, an annealing step was performed at 250 °C. The donor wafer was removed by grinding, followed by wet etching, leaving the device Si of the SOI donor wafer as the top layer.

**Device fabrication.** *Photonics.* Fabrication of photonic devices started with epitaxial deposition of 225 nm BTO on a 4 nm STO buffer on an SOI wafer with 100 nm top Si. The BTO and top Si layers were transferred by direct wafer bonding to a high-resistivity wafer with a 2-μm-thick thermal oxide. Photonic waveguides and grating couplers were fabricated by patterning the top Si layer using inductively coupled plasma (ICP) etching. After waveguide fabrication, the devices were annealed in O<sub>2</sub> at 400 °C for 4 h to reduce propagation losses to  $\sim 10$  dB cm<sup>-1</sup> (Supplementary Note 9). Electrodes were deposited in a metallization step. A SiO<sub>2</sub> cladding was deposited by plasma-enhanced chemical vapour deposition, in which vias were etched by ICP followed by the final metallization. The width of the waveguides was chosen to be 0.75 and 1.25 μm to ensure single-mode TE and TM operation, respectively. Single-mode operation was verified by simulating the 2D mode profiles with PHOENIX and COMSOL. Racetrack resonators with 50 μm (TE) and 75 μm (TM) bend radii and 75-μm-long straight sections were fabricated along with ring modulators with varying radii.

**Plasmonics.** The photonic components of the plasmonic devices were fabricated in the same way as the photonic devices (using 80 nm BTO deposited on an SOI wafer with 220 nm top Si). After patterning of photonic regions, the plasmonic waveguides were etched into the BTO using ion beam etching. After structuring of the BTO, the electrodes were deposited by a self-aligned metallization process. The propagation losses of the plasmonic structures are  $\sim 1.4$  dB μm<sup>-1</sup> (Supplementary Note 9).

**Device characterization.** *Photonics.* Optical fibres and integrated grating couplers were used to first couple light emitted from a tunable diode laser at a wavelength of  $\sim 1,550$  nm into the active devices, and afterwards out of the chip to detect the transmitted power. Applying a voltage to the electrodes creates an electric field in the BTO layer (Supplementary Note 2), which results in a modification of the refractive index because of the Pockels effect. For photonic devices, we tracked these modifications by recording the transmission spectra of the resonators as a function of the bias voltage applied. The change in the refractive index of the BTO layer can be determined from the change in the resonance wavelength  $\lambda_0$  (Supplementary Note 10). For hysteresis measurements, we iteratively changed the bias and recorded transmission spectra with a delay of  $\sim 10$  s. We acquired the frequency dependence of the EO response by modulating the applied voltage from 50 MHz to 40 GHz. We recorded the  $S_{21}$  parameter of a TE ring modulator with a radius of 15 μm using a vector network analyser while scanning  $\lambda$  across the resonance and measuring the modulated optical power at a high-speed detector with a 3 dB cutoff frequency of 33 GHz (Supplementary Note 10 and Supplementary Fig. 22) after amplifying, filtering and attenuating the modulated signal (Supplementary Note 10 and Supplementary Fig. 19). Note that the values reported for the  $S_{21}$  parameters (Fig. 3b) are extracted off resonance to minimize effects from the finite photonic lifetime on the EO bandwidth (Supplementary Note 10 and Supplementary Fig. 21). The nonlinear distortion of the EO response by the erbium-doped fibre amplifier (EDFA) operated close to saturation is considered in the data analysis, but results in inaccuracies that prevent accurate quantitative analysis of the change in refractive index from the  $S_{21}$  parameters (Supplementary Note 10).

**Plasmonics.** To characterize the plasmonic phase shifters, we applied a bias voltage of about 2.5 V and a radiofrequency signal of approximately 10 dBm at frequencies  $f_{RF}$  between 15 and 65 GHz directly to the electrodes of the phase shifters, and recorded the optical spectrum using an optical spectrum analyser. The modulation amplitude was measured as the power ratio between the optical carrier and the modulation sidebands at  $f_0 \pm \Delta f_{RF}$ . We calibrated the radiofrequency power at the

input of the radiofrequency probe and subtracted the losses of the probe based on the data sheet supplied. To measure the frequency response of plasmonic devices at frequencies lower than 15 GHz, a lightwave component analyser was used to record the  $S_{21}$  parameter of an MZM consisting of two plasmonic phase shifters between 100 MHz and 25 GHz. The overlap between the  $S_{21}$  parameter and the phase shifter modulation in the 15–25 GHz range was used to normalize the phase shifter modulation to the  $S_{21}$  parameter.

To determine the angular dependence, devices with orientations between 0° and 45° were measured with a 30 GHz radiofrequency signal. The hysteresis measurement was performed on a single device by varying the bias voltage, while keeping the radiofrequency signal constant. Based on the modulation amplitude and the applied radiofrequency power, we extracted the modulation index as described in ref. <sup>53</sup>. From the modulation index, we calculated the change in the mode index. For an improved comparison with the photonics measurements, we inverted one wing of the butterfly-shaped hysteresis loop to obtain the hysteresis loop shown in Fig. 3e.

**Datacom experiments.** *Photonics.* A TE photonic ring modulator with a radius of 12.5 μm, a coupling gap of 0.35 μm and an electrode gap of 2.75 μm was used to characterize the high-speed data transmission capability, whereby a non-return-to-zero (NRZ) pseudorandom binary sequence of length 2<sup>7</sup>–1 delivered by a bit pattern generator was applied, connected to an external clock. The modulating signal was applied by high-speed ground-signal-ground radiofrequency probes to the electrodes. The modulated optical signal was then optically amplified by an EDFA, filtered with an optical filter, and finally photodetected before its visualization at the digital communication analyser. A 40 Gbit s<sup>-1</sup> signal was thus generated (Supplementary Note 10 and Supplementary Fig. 23).

**Plasmonics.** A plasmonic phase shifter with a 50-nm-wide and 10-μm-long plasmonic waveguide was used for binary phase-shift keying (BPSK) data modulation. An electrical 50 Gbit s<sup>-1</sup> signal was generated and amplified before being applied to the modulator. The applied radiofrequency voltage peak was 0.8 V at a 50 Ω system, and the d.c. bias voltage was 2.5 V. A tunable laser, set to 1.55 μm, amplified through an EDFA to 16 dBm, was used for the optical input. After the modulator, the optical signal was re-amplified through an EDFA, fed to an optical coherent receiver and recorded by a digital sampling oscilloscope (160 GSa s<sup>-1</sup>, 63 GHz, 3 dB bandwidth). The digitized signal was processed offline, including timing recovery, carrier recovery, least mean square (LMS) equalization, symbol decision and error counting (Supplementary Note 11 and Supplementary Fig. 24).

**Simulations.** *Photonics.* All simulations were performed with a MEEP finite difference time domain (FDTD) solver. The calculations were performed using 2D FDTD with a cell size of 8.6 μm (y:z) using 33 nm grid size and 1-μm-thick perfectly matched layer (PML) boundary conditions. The simulation geometry consisted of a SiO<sub>2</sub> bottom layer, 225 nm BTO and a 100-nm-thick and 1,250/750-nm-wide Si ridge layer cladded with air. The Gaussian-shaped source was positioned in the centre of the waveguide, and the size of the source was equal to the dimensions of the waveguide (width of 750/1,250 nm, height of 325 nm). The wavelength range was set to 1,430–1,670 nm. The simulated EO response of the photonic devices was compared with the experimental data to extract the elements of the Pockels tensor (Supplementary Notes 5 and 6).

**Plasmonics.** All simulations were performed with COMSOL Multiphysics. Eigenmodes were calculated in 2D finite element method simulations with a simulated region of 500:2,000 nm<sup>2</sup> (width:height) and five mesh cells per effective wavelength in the simulated materials. The metal surface was meshed with 1.5 nm vertex spacing. First-order scattering boundary conditions were used. The simulation environment consisted of a 1,000 nm SiO<sub>2</sub> bottom layer, 20 nm Al<sub>2</sub>O<sub>3</sub>, 76 nm BTO, 38 nm BTO slab and metal electrodes, and 1,000 nm air cladding. The geometry was adapted to the TEM imaging of devices as fabricated and characterized. Simulations were performed at  $\lambda = 1,550$  nm. Material data obtained from ellipsometry was used for BTO and Au (Supplementary Note 1).

## Data availability

The data that support the findings of this study are available from the corresponding authors upon reasonable request.

## References

- 53. Shi, Y., Yan, L. & Willner, A. E. High-speed electrooptic modulator characterization using optical spectrum analysis. *J. Lightwave Technol.* **21**, 2358 (2003).